

Supporting Information for

**Biomass-Derived Wearable Energy Storage Systems Based on  
Poplar Tree-Cotton Fibers Coupled with Binary Nickel-Cobalt  
Nanostructures**

Farzaneh Hekmat<sup>1,2,3</sup>, Husnu Emrah Unalan<sup>1,2\*</sup>, Saeed Shahrokhian<sup>3\*</sup>

## Supplementary Materials

### **Biomass-Derived Wearable Energy Storage Systems Based on Poplar Tree-Cotton Fibers Coupled with Binary Nickel-Cobalt Nanostructures.**

Farzaneh Hekmat<sup>1,2,3</sup>, Husnu Emrah Unalan<sup>1,2\*</sup>, Saeed Shahrokhian<sup>3\*</sup>

Prof. H. E. Unalan and Dr. F. Hekmat, Department of Metallurgical and Materials Engineering, Middle East Technical University, Ankara 06800, Turkey  
E-mail: Unalan@metu.edu.tr

Prof. S. Shahrokhian, and Dr. F. Hekmat, Department of Chemistry, Sharif University of Technology, Tehran 11155-9516, Iran  
E-mail: Shahrokhian@sharif.edu

Prof. H. E. Unalan and Dr. F. Hekmat, Energy Storage Materials and Devices Research Center (ENDAM), METU, Ankara 06800, Turkey

**Keywords:** Asymmetric Supercapacitors; Unwoven Poplar Tree-Cotton; Nickel-Cobalt Oxide; Single Wall Carbon Nanotubes; Iron Oxide

- S1 Chemicals
- S2 Equipment and Materials Characterization
- S3 Electrochemical Measurements
- S4 Preparation of Ni-Co-O@CF based Positive Electrodes
- S5 Preparation of Fe<sub>2</sub>O<sub>3</sub>-SWCNTs@CF based Negative Electrodes
- S6 Supercapacitor Device Fabrication
- S7 SEM Characterization of Bare Cotton Fibers (CFs)
- S8 SEM Characterization of Ni-Co-O NR Decorated CFs
- S9 TEM Characterization of Ni-Co-O NR Decorated CFs
- S10 Electrochemical Characterization of Ni@Pd-activated CFs
- S11 Cycle Stability of Ni-Co-O@CF Positive Electrodes
- S12 Material and Structural Characterization of Fe<sub>2</sub>O<sub>3</sub>-SWCNTs@CF Electrodes
- S13 Electrochemical Characterization of Fe<sub>2</sub>O<sub>3</sub>-SWCNTs@CF Electrodes
- S14 Cycle Stability of Fe<sub>2</sub>O<sub>3</sub>-SWCNT@CF Negative Electrodes
- S15 Cycle Stability of Ni-Co-O@CF SSC Devices
- S16 Cycle Stability of Ni-Co-O@CF//Fe<sub>2</sub>O<sub>3</sub>-SWCNT@CF ASC Devices
- S17 Comparison of Electrode and Device Properties with Literature

## 1. Experimental Section:

**S1 Chemicals:** All chemical reagents were of analytical grade and directly used without further purification. Palladium (II) chloride, ammonia (solution 30% in water), hydrazine hydrate (solution 35% in water), hydrochloric acid, nickel (II) sulfate hexahydrate, nickel (II) chloride hexahydrate, boric acid, nickel (II) nitrate hexahydrate, cobalt (II) nitrate hexahydrate, urea, iron (III) chloride hexahydrate, ammonium oxalate monohydrate, sulphuric acid, nitric acid, acetone, ethanol, potassium hydroxide, polyvinyl alcohol (PVA), and Triton X-100 were obtained from Merck (Germany). SWCNTs and 1-methyl-3-octadecylimidazolium chloride ( $[C_{18}C_1Im]Cl$ ) were supplied by Carbon Solutions, Inc. (USA) and KimiaExir (Iran), respectively. Deionized water (DIW, 18 M $\Omega$ ) was used for the experiments obtained from a Zeneer power I water purification system (Human Corp., Korea).

**S2 Equipment and Materials Characterization:** A DC power supply (D605, DAZHENG DC, China) was employed to provide the electric field for not only electroplating of Ni, but electrodeposition of Fe<sub>2</sub>O<sub>3</sub>. Probe sonicator (HD 2070, Bandelin Sonopuls) was used to prepare the well-dispersed suspension of SWCNTs. Structural characterisation was conducted by employing field-emission scanning electron microscope (FE-SEM) (TESCAN, Mira III LMU, Czech Republic), equipped with an energy dispersive spectroscopy (EDS) probe, X-ray diffraction (XRD) (RIGAKU D/MAX-IIIC diffractometer, D8 Advance using the Cu K $\alpha$  radiation, Bruker, Germany), Raman spectroscopy (iHR550, HORIBA Ltd., Japan), Fourier-transform infrared spectroscopy (FT-IR) (Spectrum 100 Optica FT-IR Spectrometer, PerkinElmer, USA), and X-ray photoelectron spectroscopy (XPS) (PHI 5000 VersaProbe III, using Al X-ray source, Physical Electronics, Inc, USA). Thermo-gravimetric analysis (TGA) was performed with a thermo-gravimetric analyzer (Exstar SII TG/DTA

7300, Latvia). The measurements were carried out in the temperature range of 24–800 °C, with a heating rate of 10 °C min<sup>-1</sup> under air flow (30 cm<sup>3</sup> min<sup>-1</sup>).

**S3 Electrochemical Measurements:** Electrochemical performance of both binder-free Ni-Co-O core/shell-like decorated CFs as the positive and Fe<sub>2</sub>O<sub>3</sub>-CNTs@CF as the negative electrode, were investigated in 3 M KOH solution at room temperature. A three-electrode configuration was used with a mercury-mercury oxide (Hg/HgO) reference electrode and a platinum sheet as the counter electrode. Cyclic voltammetric (CV) measurements were conducted in a potential range between -0.2 to +0.4 V for the cathode and -0.6 to 0 V for the anode (vs. a Hg/HgO reference electrode) at scan rates of 1 to 70 mV s<sup>-1</sup> and 1 to 100 mV s<sup>-1</sup>, respectively.

Galvanostatic charge/discharge (GCD) measurements were performed at different current densities within the same voltage window for the CV analysis, and the cyclic stability was characterized up to 4000 cycles for each individual positive (Ni-Co-O@CF) and negative (Fe<sub>2</sub>O<sub>3</sub>-CNTs@CF) electrodes. Electrochemical impedance spectroscopy (EIS) was conducted to confirm the capacitive performance at the open circuit potential (OCP), applying an alternating potential with an amplitude of 5 mV within the frequency range of 100 kHz to 0.01 Hz. Capacitive performance of the Ni-Co-O@cotton SSC and Ni-Co-O@cotton//Fe<sub>2</sub>O<sub>3</sub>-CNTs@cotton-based ACS was investigated by CV and GCD with opening potential windows of 0.6 and 1.2 V, respectively. The cycle stability of the fabricated supercapacitors was studied under 4000 continuous charge-discharge cycles. All electrochemical tests were performed under ambient conditions.

The specific capacity (Cg<sup>-1</sup>) values were obtained according to the following equation<sup>1-4</sup>.

$$Q = \frac{\int I \times dt}{m \times 3.6} \quad (S1)$$

, where  $I$  (A) and  $\Delta t$  (s) are the discharge current and corresponding time, and  $m$  (g) is the mass of the active materials loaded onto the CFs.

The specific capacitance of the fabricated Ni-Co-S NRs@cotton//Ni-Co-S NRs@cotton SSC and battery-type Ni-Co-S NRs@cotton//Fe<sub>2</sub>O<sub>3</sub>-CNTs@cotton ASC device can be estimated from the following equations<sup>1-5</sup>:

$$C_{cell} = \frac{I \times \Delta t}{M \times \Delta V} ; M = m_{anode} + m_{cathode} \quad (S2)$$

$$Q_{cell} = \frac{\int I \times dt}{M \times 3.6} ; M = m_{anode} + m_{cathode} \quad (S3)$$

, in which  $C_{cell}$ ,  $Q_{cell}$ ,  $I$  (A), and  $t$  (s) are the cell capacitance and capacity, discharge current, and time, respectively.  $M$  is the total mass of active materials deposited on both positive and negative electrodes.

The energy and power density ( $E$  and  $P$ ) values of the fabricated supercapacitors are calculated using the following equations<sup>6-8</sup>.

$$E = \frac{C \times \Delta V^2}{2 \times 3.6} \quad (S4)$$

$$P = \frac{E \times 3.6}{\Delta t} \quad (S5)$$

, where  $E$ ,  $C$ ,  $\Delta V$ ,  $P$ , and  $\Delta t$  are the energy density (Wh.kg<sup>-1</sup>), specific capacitance (Fg<sup>-1</sup>), potential window (V), power density (kW.kg<sup>-1</sup>), and discharge time (s), respectively.

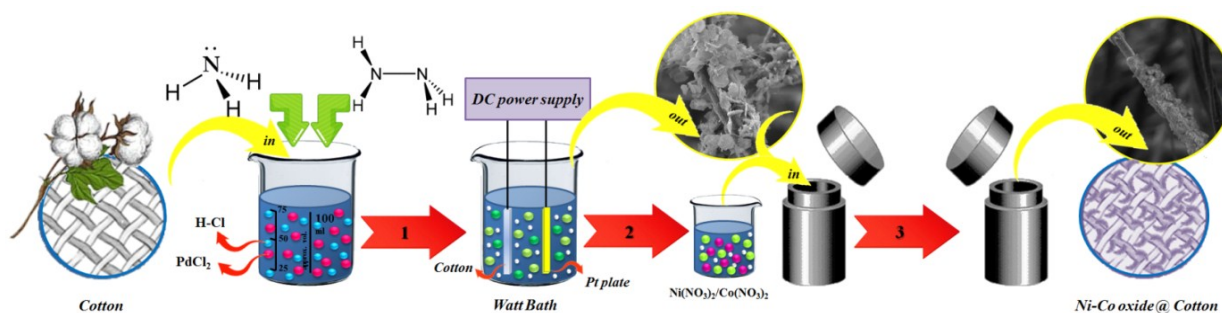
**S4 Preparation of Ni-Co-O@CF based Positive Electrodes:** A schematic illustration of the positive electrode preparation is provided in Scheme S1. Unwoven poplar tree CFs were first precleaned by rinsing with Triton X-100 as a non-ionic detergent for 20 min at 40 °C. The precleaned unwoven CFs were further cleaned using DIW and dried under vacuum at 50 °C overnight. The degreased unwoven CFs were then knitted together in a tapestry

structure, which was pre-treated by dimethylformamide, acetone, ethanol, and DIW using an ultrasonicator. The knitted cotton-based substrate was then prepared and degreased in acetone, ethanol, and DIW under ultrasound waves, respectively. The prepared cotton-based substrate was then dried under vacuum at 50°C overnight. In a typical procedure, a thin layer of Pd active layer was deposited onto the prepared knitted cotton substrate via a chemical bath plating process, during which the knitted cotton-based substrate was immersed in a 50 mL solution containing PdCl<sub>2</sub> (0.015 M), HCl (solution 0.3% in water), ammonia (solution 30% in water), and hydrazine hydrate (0.005 M) for 30 min at 60°C. The Pd activated CFs were then washed in DIW and ethanol, and dried at 50°C for 12 h under vacuum.

Afterward a 50 ml Watts bath composed of 320 mM NiSO<sub>4</sub>, 80 mM NiCl<sub>2</sub>, and 280 mM H<sub>3</sub>BO<sub>3</sub> was prepared. Subsequently, the pH value of the solution was adjusted to 2.0 by adding H<sub>2</sub>SO<sub>4</sub>. The electrochemical deposition of Ni on the prepared Pd-activated cotton substrate was then conducted in a three-electrode configuration, where the cotton substrate, Pt plate, and Ag/AgCl was used as the working, counter, and reference electrodes, respectively. All the potentials were referred to the Ag/AgCl reference electrode. The electrodeposition process was conducted within the potential range of -1.1 to 0 V with a constant potential sweep rate of 50 mVs<sup>-1</sup>. The prepared Ni-Pd activated CF electrode was then dried at 50 °C under vacuum for 12 h.

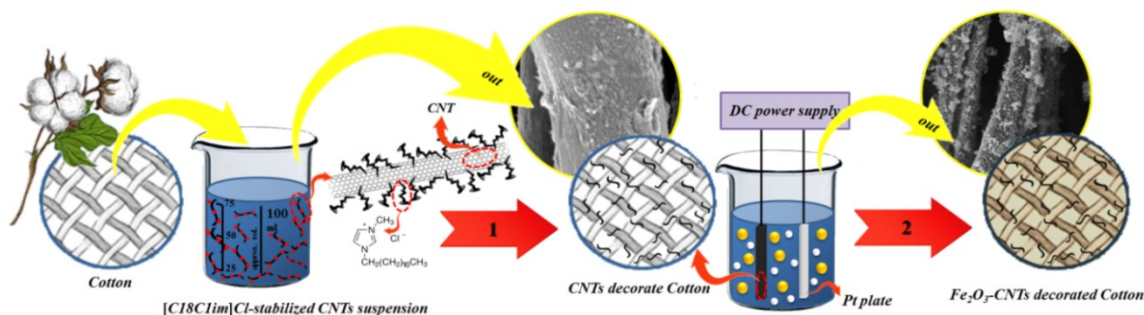
The Ni-Pd-activated CFs were directly decorated by Ni-Co-O NRs via a one-pot hydrothermal method at a relatively low temperature. Prior to the hydrothermal process, a 75 ml aqueous solution containing Co(NO<sub>3</sub>)<sub>2</sub>.6H<sub>2</sub>O (8 mmol), Ni(NO<sub>3</sub>)<sub>2</sub>.6H<sub>2</sub>O (4 mmol), and urea (15 mmol) was prepared. The prepared solution was homogenized for 30 min using an ultrasonic bath. The prepared pinkish solution was then transferred to a 100 ml Teflon-lined stainless steel autoclave where the activated cotton-based fibers were simply immersed into the prepared solution. Afterward, the autoclave was sealed and kept at 120 °C for 6 h. At the

end of the reaction and cooling down to room temperature, the prepared electrode was washed with DIW and ethanol several times and dried overnight under vacuum at 50 °C. This electrode was labeled as Ni-Co-O@CFs and the mass loading of the electrode active materials was measured as 2 mg.cm<sup>-2</sup>.



**Scheme S1.** Schematic illustration for the fabrication process of the Ni-Co-O@CF electrodes.

**S5 Fabrication of the Fe<sub>2</sub>O<sub>3</sub>-SWCNTs@CF based Negative Electrodes:** The fabrication process for the negative electrode is schematically illustrated in Scheme S2. The well-dispersed suspensions of SWCNTs were prepared by adding 4 mg SWCNTs into 10 ml of [C<sub>18</sub>C<sub>1</sub>im]Cl aqueous solution. Afterward, the solution was sonicated for 10 min by a probe sonicator. The prepared suspension was centrifuged at 5000 rpm for 10 min to sediment large bundles, after keeping at room temperature without any perturbation for 24 h. The prepared cotton substrate was dipped into the SWCNTs suspension for 5 min and then dried at 80 °C for 10 min in an oven. This procedure was repeated 5 times and the SWCNT@cotton electrode was finally dried under vacuum overnight. Afterward, the prepared SWCNTs@CF sample was placed in 2M HNO<sub>3</sub> for 5 h to remove the IL [9, 10] and air-dried. The sample was then placed into a DIW bath at 70-80 °C for 30 min and dried at 50 °C overnight under vacuum. The electrodeposition of ferric oxide was initiated by the preparation of a homogeneous solution containing FeCl<sub>3</sub>.6H<sub>2</sub>O (9 g.l<sup>-1</sup>) and (NH<sub>4</sub>)<sub>2</sub>C<sub>2</sub>O<sub>4</sub>.H<sub>2</sub>O (14 g.l<sup>-1</sup>), which was sonicated for 30 min. Subsequently, ferric oxide nanostructures were directly electrodeposited onto the prepared SWCNTs@CFs.



**Scheme S2.** Schematic illustration for the fabrication process of Fe<sub>2</sub>O<sub>3</sub>-SWCNTs@CF electrodes. **Sch**

A cathodic electrodeposition process was used to fabricate Fe<sub>2</sub>O<sub>3</sub>-CNTs@Cotton-based electrodes under a constant current density of 4 mA.cm<sup>-2</sup> for 30 min at room temperature. A Pt plate was used as the anode. Following electrodeposition, Fe<sub>2</sub>O<sub>3</sub>-SWCNTs@CFs was rinsed with DIW and dried under vacuum at 50 °C. The fabricated electrode was labeled as Fe<sub>2</sub>O<sub>3</sub>-SWCNTs@CF electrode and the mass loading of the electrode active materials was measured as 4.3 mg.cm<sup>-2</sup>.

**S6 Supercapacitor Device Fabrication:** Compared to conventional electrolytes, polymer gel electrolytes not only provide flexibility and foldability but also reduce the short circuit probability for wearable supercapacitors. Accordingly, an alkaline polymer gel electrolyte was prepared using the sol-gel method. Initially, polyvinyl alcohol (PVA) was dissolved in deionized water through continuous stirring for about 4 h at 80 °C to form a clear gel-like solution [11]. Afterward, the alkaline electrolyte was added slowly into the resulting solution while the solution was stirred continuously. A homogeneous viscous solution was, therefore, achieved. The masses of both negative and positive electrodes were balanced. The SSC was assembled using two Ni-Co-O@CF electrodes; meanwhile, the ASC device was assembled using a Ni-Co-O@CF and a Fe<sub>2</sub>O<sub>3</sub>-CNTs@CF electrode as cathode and anode, respectively.

**S7 SEM Characterization of Bare Cotton Fibers (CFs):**

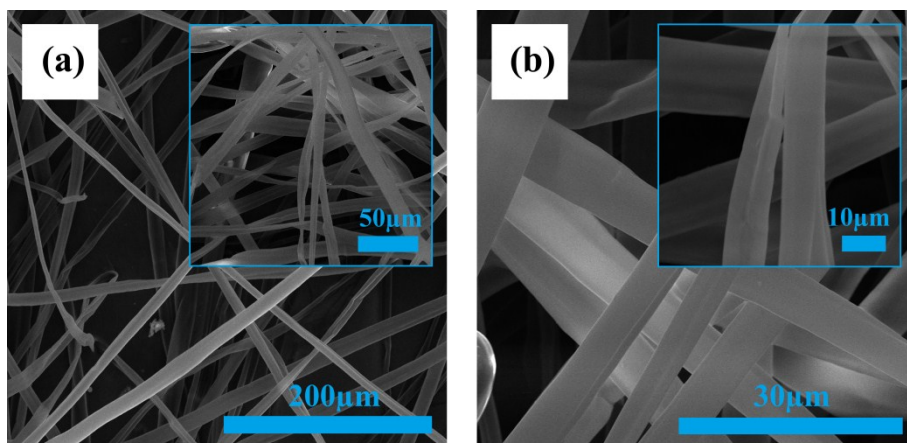


**Figure S1.** (a) and (b) surface morphology of bare cotton fibers at different magnifications.

**S8 SEM Characterization of Ni-Co-O NR Decorated CFs:**

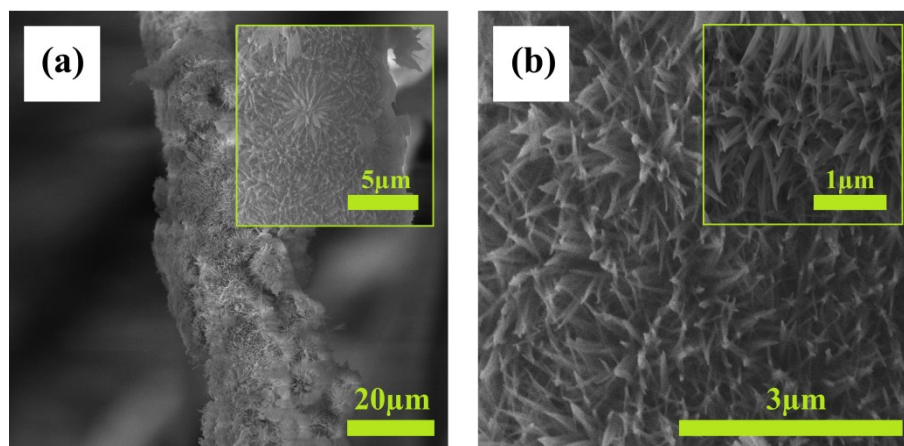


**Figure S2.** (a) and (b) SEM images of Ni-Co-O core/shell-like decorated CFs at different magnifications.

**S9 TEM Characterization of Ni-Co-O NR Decorated CFs:**

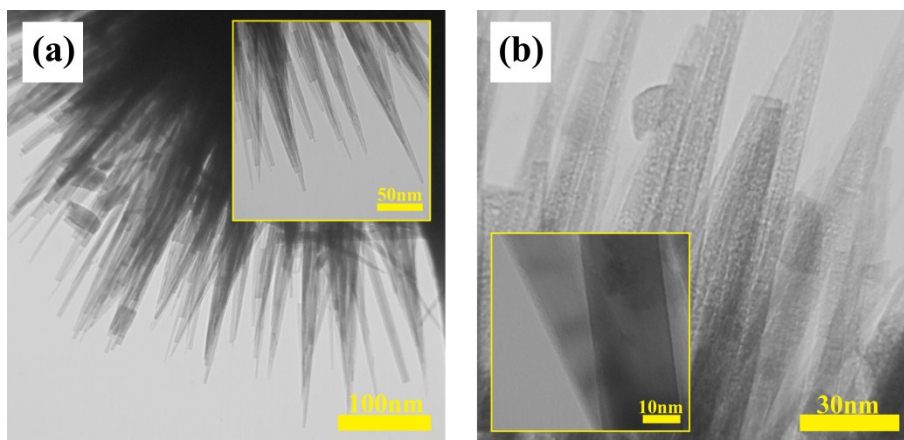


**Figure S3.** (a) and (b) TEM images of Ni-Co-O NRs at different magnifications.

### *S10 Electrochemical Characterization of Ni@Pd-activated CFs:*

Having a critical role on the electrochemical performance of the fabricated electrodes, evaluation of the supercapacitive behavior of Ni@Pd-activated CF substrates is of prime significance. Accordingly, the electrochemical features of the Ni coated Pd-activated CFs were investigated using CV, GCD, and EIS techniques in a 3-electrode configuration using 3M KOH electrolyte at room temperature. CV curves of Ni@Pd-activated CFs at different scan rates, increasing from 10 to 70  $\text{mVs}^{-1}$ , are shown in Figure S4 (a). Figure S4 (b) provides clear evidence on an improved electrochemical performance of the fabricated Ni-Co-O@CF electrodes in comparison to Ni@Pd-activated CFs, which can be attributed to the enhanced ion diffusion path as a direct result of integral decoration of CFs with core/shell-like Ni-Co-O NRs <sup>6</sup>.

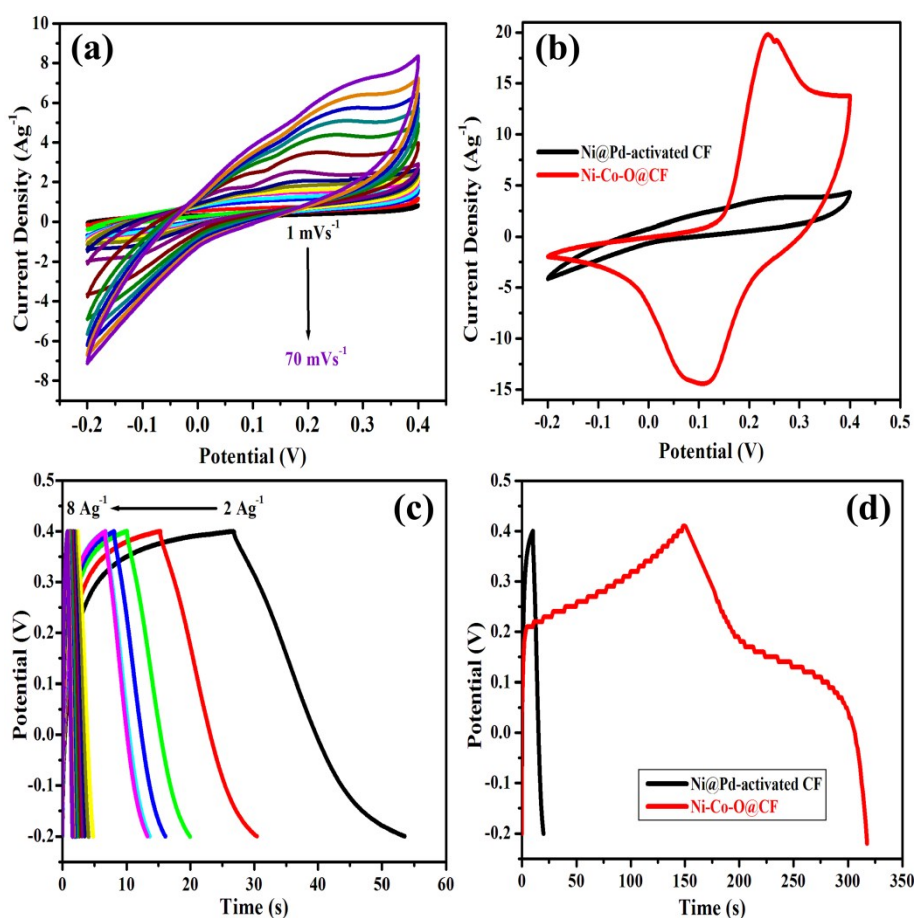


**Figure S4.** (a) The CVs of the Ni@Pd-activated CF electrode at different scan rates increasing, (b) the CVs of Ni@Pd-activated CF (black CV) was compared with the Ni-Co-O@CF electrodes (red CV) at the scan rate of 50  $\text{mVs}^{-1}$ , (c) GCD curves of the Ni@Pd-activated CF electrodes, and (d) the GCD curves of Ni@Pd-activated CF electrode (black) was compared to the Ni-Co-O (red) ones at a constant current density of 3  $\text{Ag}^{-1}$ .

The electrochemical performance of the Ni@Pd-activated CF electrode was further studied using GCD technique. GCD measurements conducted within a potential range of -0.2 to +0.4 V at different current densities ranging from 2 to 8 Ag<sup>-1</sup> (Figure S4 (c)). As seen in the figure, a good agreement between GCD curves and CVs was observed. Receiving benefit from remarkable reversibility, Ni@Pd-activated CFs represents symmetric charge-discharge curves within a broad range of current densities. A negligible voltage drop at the start point of the discharge curves attributed to the reasonable equivalent series resistance (ESR) of the Ni@Pd-activated CFs, assuring a relatively rapid ion transport at the surface of the electrodes. The GCD curve of Ni-Co-O decorated CF electrodes (red) is compared to Ni@Pd-activated CFs (black) in Figure S4 (d). In good agreement with the CV results, redox peak position changes in Ni-Co-O@CF electrodes compared to the substrate (Ni@Pd-activated CFs) and enhanced capacitive performance of the core/shell-like Ni-Co-O@CF electrodes come into view in Figure S4 (d). The specific capacities of Ni@Pd-activated CFs were estimated at different current densities.

As shown in Figure S5 (a), upon increasing the current density from 2 to 8 Ag<sup>-1</sup> (almost over 4 times), the Ni@Pd-activated CFs was still able to retain about 40% of their initial capacity.

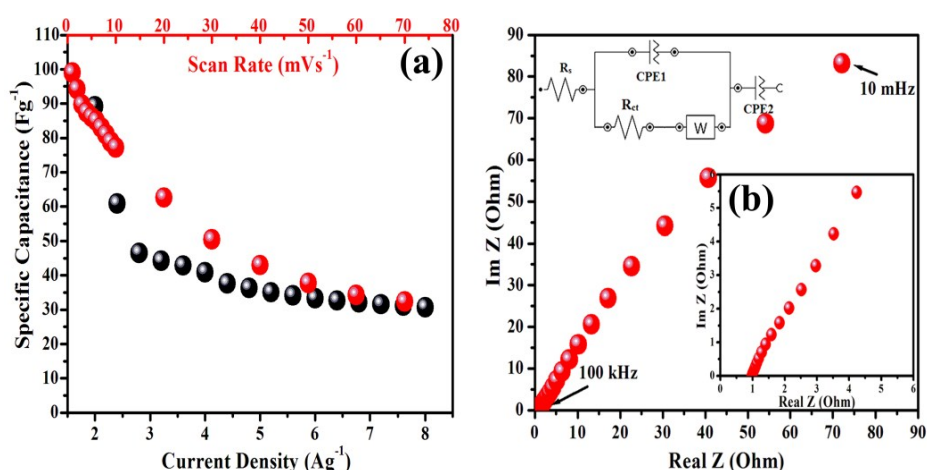


**Figure S5.** (a) The dependence of the gravimetric capacity of the Ni@Pd-activated CF electrodes on the applied current density (bottom axis-black) and scan rate (top axis-red), (b) Nyquist plot of Ni@Pd-activated CF electrode over a frequency range of 100 kHz to 10 mHz. The inset shows the magnified data in the high-frequency range and the corresponding equivalent circuit model.

The Nyquist plot of Ni@Pd-activated CFs and its corresponding enlargement of the high-frequency region together with the corresponding equivalent circuit model, derived from electrochemical impedance spectroscopy (EIS) analysis are presented in Figure S5 (b). The ESR of the Ni@Pd-activated CFs is estimated as 0.99  $\Omega$ . As a consequence of the fast charge transport rate, the Ni@Pd-activated CF electrode renders reasonable charge transfer resistance ( $R_{ct}$ ) of 0.40  $\Omega$ .

***S11 Cycle Stability of Ni-Co-O@CF Positive Electrodes:***

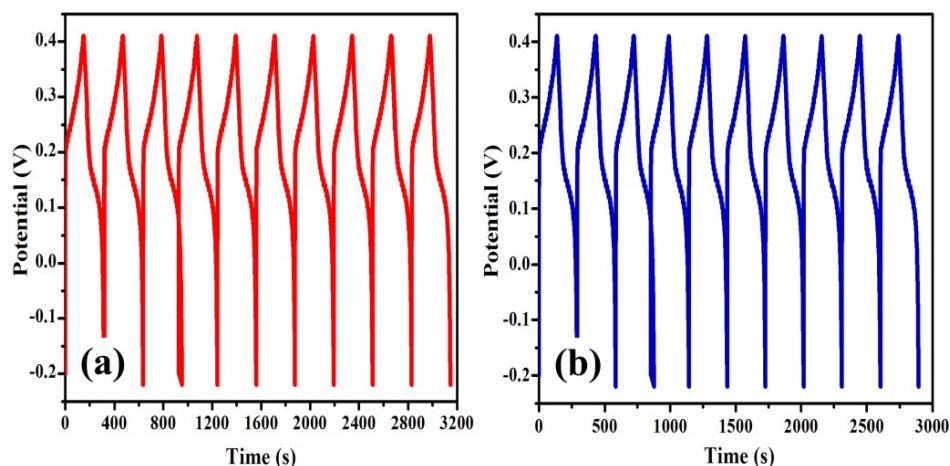


**Figure S6.** (a) The first and (b) last 10 GCD cycles of the Ni-Co-O@CF electrodes at a current density of 3Ag<sup>-1</sup>.

***S12 Materials and Structural Characterization of Fe<sub>2</sub>O<sub>3</sub>-SWCNTs@CF***

***Electrodes:*** Having a profound impact on the physicochemical feature of CNTs, especially their electrochemical performance, characterization of [C<sub>18</sub>C<sub>1</sub>im]Cl-stabilized SWCNTs is of special importance<sup>12</sup>. Figure S7 (a) shows a photograph of SWCNTs in an aqueous solution stabilized by adding [C<sub>18</sub>C<sub>1</sub>im]Cl. It can be noticed that even after 10 min of ultrasonication, SWCNTs start to agglomerate in the aqueous solution (sample A). In contrast, after adding [C<sub>18</sub>C<sub>1</sub>im]Cl into the same aqueous solution, a black homogenous dispersion was obtained, which can be kept for more than 6 months (sample B).

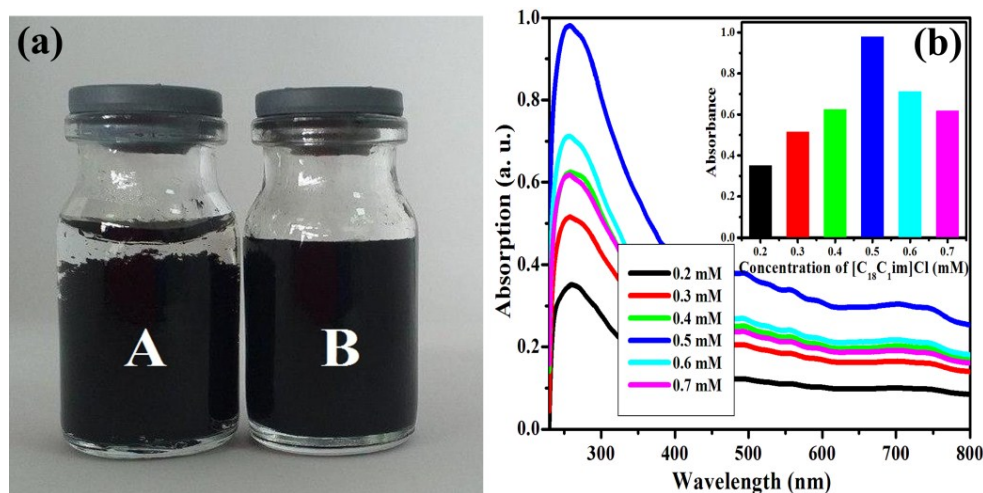


**Figure S7.** (a) Photos of aqueous SWCNT dispersions: without IL (A), imaged after 10 min and with 0.6 mM of [C<sub>18</sub>C<sub>1</sub>im]Cl (B), imaged after 6 months, (b) UV-Vis spectra of aqueous SWCNTs solution dispersed using [C<sub>18</sub>C<sub>1</sub>im]Cl of different concentrations, inset: the variation of the intensity of absorption peaks (at ~260 nm) of SWCNT suspensions vs. the concentration of [C<sub>18</sub>C<sub>1</sub>im]Cl (4 mg SWCNTs dispersed in 10 mL of different concentration of [C<sub>18</sub>C<sub>1</sub>im]Cl in aqueous solutions).

Although bundled SWCNTs are inactive in the UV-Vis region, individual CNTs exhibit a strong characteristic absorption around 260 nm<sup>13-15</sup> and an increase in absorbance of SWCNTs is expected with increasing concentration of individual SWCNTs in aqueous suspensions<sup>14</sup>. UV-Vis spectroscopy, therefore, is a suitable method which is commonly used to investigate the effect of dispersing agents in making stable suspensions of individual CNTs in aqueous solutions<sup>13-15</sup>. It is worth mentioning that [C<sub>18</sub>C<sub>1</sub>im]Cl aqueous solutions display only negligible absorptions within the wavelength from 200 to 1300 nm, consequently, the effect of ILs on the absorption of CNT suspensions in UV-Vis region can be ignored and the adsorption of IL-stabilized CNT suspensions can only be attributed to the individual SWCNTs<sup>12,13</sup>. The intensity of UV-Vis absorption peaks, in this regard, correlates tightly with the amount of individually dispersed CNTs and provides compelling evidence on the ability of different concentrations of [C<sub>18</sub>C<sub>1</sub>im]Cl in the dispersion of SWCNTs. UV-Vis spectra of SWCNT suspensions with different concentrations of [C<sub>18</sub>C<sub>1</sub>im]Cl, are shown in Figure S7 (b). As shown in the inset IL molecules get entirely adsorbed on the surface of SWCNTs at the concentrations which are slightly higher than their critical micelle

concentration (cmc). As a result, there is a linear relationship between the intensity of absorption peaks and the concentration of  $[\text{C}_{18}\text{C}_1\text{im}]\text{Cl}$  as a dispersing agent with a positive slope at low concentrations of IL<sup>14</sup>. By increasing the concentration of dispersing agent ( $[\text{C}_{18}\text{C}_1\text{im}]\text{Cl}$ ) more than their cmc, some molecules of  $[\text{C}_{18}\text{C}_1\text{im}]\text{Cl}$  start self-aggregation to form micelles and others continue adsorbing on the surface of SWCNTs<sup>13</sup>. Accordingly, the amounts of micelles increase by increasing the concentration of IL. As a result, although the concentration of IL is increased, the amount of free IL molecules in the bulk solutions is not increased<sup>13</sup>. It is clear that not only the formation of micelles around SWCNTs but also the interaction between them will be simultaneous with increasing the IL concentration, ending up in the re-aggregation of the separated SWCNTs<sup>13</sup>. All in all, it can be expected that the amount of individual SWCNTs in aqueous solutions and also the intensity of absorption peaks in the UV-Vis region decreases slowly with an increase in the concentration of IL<sup>13,14</sup>.

The structure of IL-stabilized SWCNTs (red spectrum) in comparison to pristine SWCNTs (black) and  $[\text{C}_{18}\text{C}_1\text{im}]\text{Cl}$  (blue spectrum) was further evaluated using FT-IR analysis (Figure S8 (a)). The vibration peak of adsorbed water, which appears between 3000 - 3700  $\text{cm}^{-1}$ , can be seen in all spectra. As observed in the blue spectrum, several characteristic bands of imidazolium-based ILs appear at  $\sim 3100$ ,  $\sim 2900$ , 1630,  $\sim 1570$ ,  $\sim 1170$ ,  $\sim 850$ ,  $\sim 750$  and  $\sim 620$   $\text{cm}^{-1}$ , which can be attributed to the imidazole ring  $\nu(\text{C-H})$ , aliphatic  $\nu(\text{C-H})$ , O-H bending, imidazole ring stretching, imidazole H-C-C and H-C-N bending, in-plane imidazole ring bending, out-of-plane C-H bending of imidazole ring, and imidazole  $\text{C}_2\text{-N}_1\text{-C}_5$  bending, respectively<sup>16</sup>. In comparison to the FT-IR spectrum of  $[\text{C}_{18}\text{C}_1\text{im}]\text{Cl}$  (blue spectra), it is clear that the characteristic peaks of IL became broader and less intense with a red-shift in the FT-IR spectrum of  $[\text{C}_{18}\text{C}_1\text{im}]\text{Cl}$ -stabilized SWCNTs (red spectrum). The peak shifts are associated with the charge transfer between IL and SWCNTs<sup>12</sup>. Moreover, the red-shift observed in the IL-stabilized SWCNTs can be attributed to the hydrophobic interactions

between SWCNTs and the hydrocarbon chain of IL <sup>12</sup>. Additionally, the characteristic peaks of CO groups and C=C bands within the spectrum of pristine SWCNTs (black) at  $\sim 2200\text{ cm}^{-1}$  and within  $1400\text{-}1600\text{ cm}^{-1}$  region, respectively, disappeared in the FT-IR spectrum of IL-stabilized SWCNTs (red spectrum) <sup>6</sup>. Therefore, FT-IR clearly demonstrated that the  $[\text{C}_{18}\text{C}_1\text{im}]\text{Cl}$ -based ILs molecules were tightly adsorbed on the surface of SWCNTs with no significant changes in the structure of both ILs and SWCNTs <sup>12</sup>.

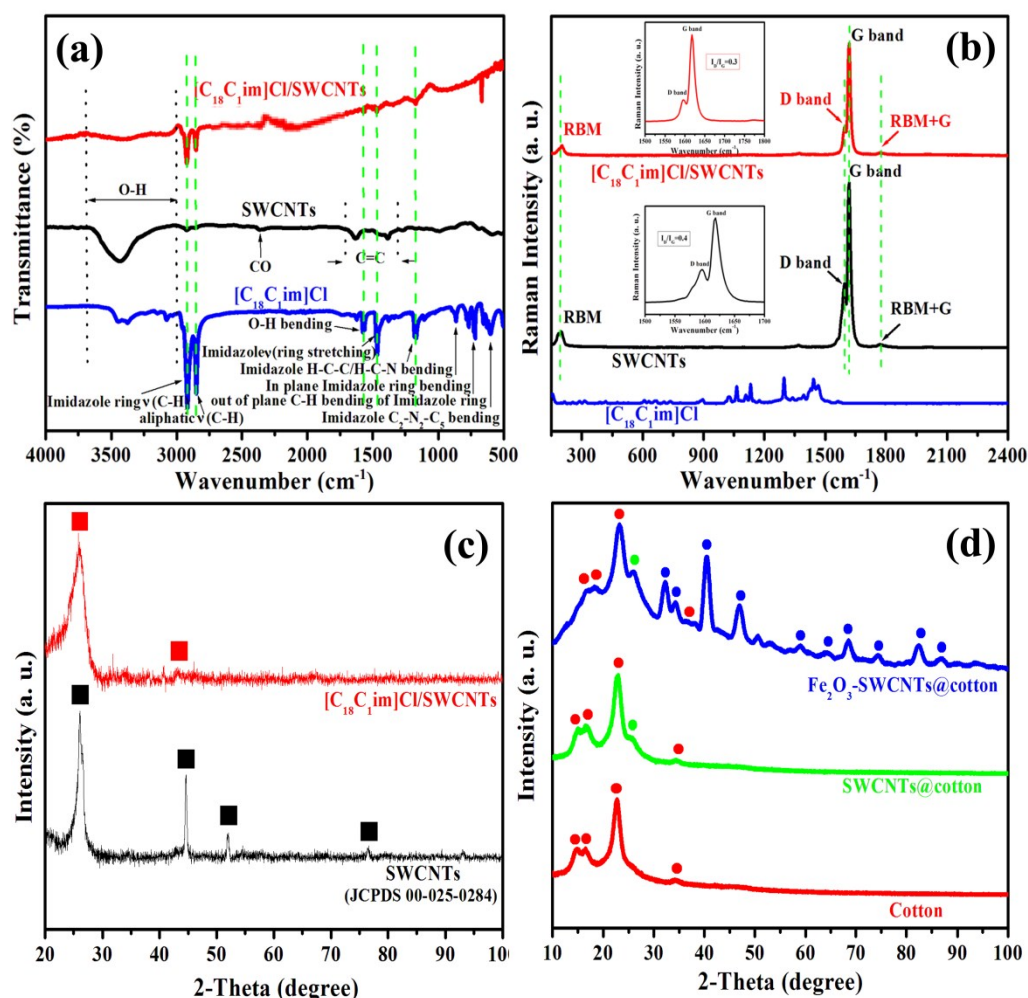


**Figure S8.** (a) FT-IR spectra of  $[\text{C}_{18}\text{C}_1\text{im}]\text{Cl}$  (blue), compared with pristine SWCNTs (black) and affected by  $[\text{C}_{18}\text{C}_1\text{im}]\text{Cl}$  ones (red), (b) Comparative Raman spectra of SWCNTs/ $[\text{C}_{18}\text{C}_1\text{im}]\text{Cl}$  (red), pure SWCNTs (black), and  $[\text{C}_{18}\text{C}_1\text{im}]\text{Cl}$  (blue), (c) XRD patterns for pristine SWCNTs (black), and SWCNTs which affected by  $[\text{C}_{18}\text{C}_1\text{im}]\text{Cl}$  (red), (d) XRD patterns of CFs (red) and SWCNTs@CFs (green) compared with  $\text{Fe}_2\text{O}_3$ -SWCNTs@CFs (blue).

Raman spectroscopy is commonly used to investigate the degree of changes in the structure of SWCNTs following IL dispersion <sup>17</sup>. In Figure S8 (b), the Raman spectra of SWCNTs Bucky gel prepared using a small amount of 1-methyl-3-octadecylimidazolium

chloride, is compared to the corresponding IL ( $[\text{C}_{18}\text{C}_1\text{im}]\text{Cl}$ ). According to the previous studies, non-covalent surface modifications of SWCNTs with ILs only slightly change the structure of SWCNTs and cause minimum structural damage to SWCNTs, which is a clear advantage in retaining the unique properties of SWCNTs, such as high electrical conductivity, high charge transport capability, high electrochemical stability<sup>17,18</sup>. Therefore, no significant changes in the Raman spectra of SWCNTs after dispersing with  $[\text{C}_{18}\text{C}_1\text{im}]\text{Cl}$  is expected. As can be seen from Figure S8 (b), the characteristic peaks of IL vanished when used as a dispersing agent to prepare Bucky gel<sup>18-20</sup>. The G and D bands are the two most distinguishing features of CNTs in Raman spectra. They are attributed to the graphitic  $\text{E}_{2g}$  optical mode known as G band corresponding to the  $\text{sp}^2$  hybridized carbons in the structure of graphite, and D band is attributed to  $\text{A}_{1g}$  mode of disordered graphitic structure<sup>17,19</sup>. As shown in the inset of Figure S8 (b), the change in the  $\text{I}_D/\text{I}_G$  ratio of IL-stabilized SWCNTs is insignificant compared to that of pristine SWCNTs. These results indicate the physical adsorption of ILs onto the SWCNTs without any significant change in the crystalline structure of the SWCNTs<sup>17</sup>. As a consequence,  $[\text{C}_{18}\text{C}_1\text{im}]\text{Cl}$  seems to be an ideal candidate for non-covalent surface modification of SWCNTs by retaining their unique mechanical, electrical, and thermal properties<sup>17-19</sup>.

In addition, the effect of interaction between SWCNTs and  $[\text{C}_{18}\text{C}_1\text{im}]\text{Cl}$  on the crystalline structure of SWCNTs was further investigated by XRD technique. The XRD pattern of pristine SWCNT (black spectrum) is shown in Figure S8 (c). Diffraction peaks at  $2\theta$  values of  $26^\circ$ ,  $44.7^\circ$ ,  $52^\circ$ , and  $77^\circ$ , correspond to (002), (101), (004), and (110) crystal planes (JCDPS, card no 00-025-0284), respectively. Herein, the XRD pattern for SWCNTs  $[\text{C}_{18}\text{C}_1\text{im}]\text{Cl}$  is shown with red. Compared to pristine SWCNTs (black spectrum), no significant crystallographic changes are observed in the XRD pattern of SWCNTs (except small shifts in  $2\theta$  values). This clearly indicates that the interactions between SWCNTs and

ILs caused no significant changes in the structure of SWCNTs, and signifies once more that ILs were physically adsorbed on the surface of SWCNTs<sup>21,22</sup>. Additionally, as shown in Figure S8 (d), the XRD pattern of Fe<sub>2</sub>O<sub>3</sub>-CNTs@CFs (blue spectrum) is compared to bare CFs (red) and SWCNTs@CFs (green). The characteristic peaks of CFs are observed in all spectra. The characteristic peak of CNTs, which can be indexed as (002) crystal plane, provides evidence that the CF network was decorated with CNTs (JCPDS card no. 00-025-0284). The XRD pattern for Fe<sub>2</sub>O<sub>3</sub>-SWCNTs@CFs (blue spectrum in Figure S8 (d)) signifies that the Fe<sub>2</sub>O<sub>3</sub> nanostructures were crystallized in the rhombohedral phase with R-3C space group (JCPDS card no. 01-084-0306).

The surface morphology of the SWCNTs decorated CFs was investigated using SEM and the images are provided in Figure S9 (a). The SEM images provide evidence on the successful preparation of SWCNTs@CF electrodes.

For the negative electrodes, FE-SEM images verified that the CFs were homogeneously coated with the Fe<sub>2</sub>O<sub>3</sub>-SWCNTs nanocomposite, as shown in Figure S9 (b). The elemental composition of the prepared cotton electrodes was investigated through EDS mapping and the results are provided in Figure S9 (c) and (d), showing homogenous decoration of CFs by iron oxide-SWCNTs based nanostructures.

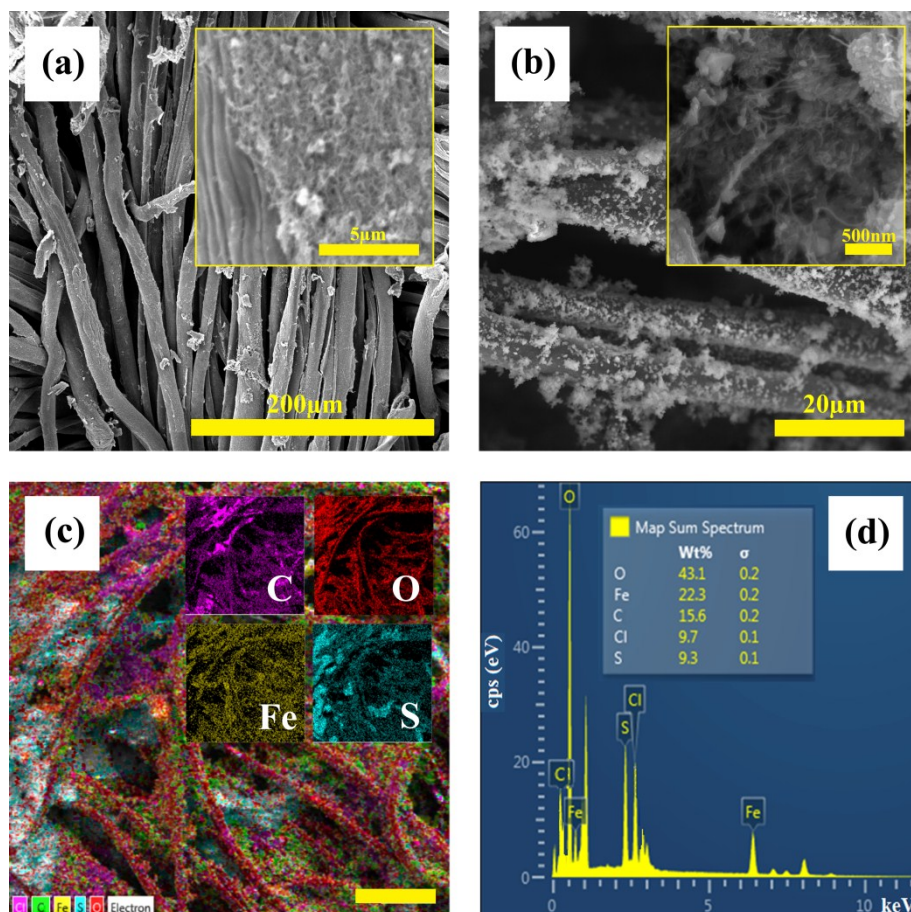


**Figure S9.** Surface morphology of (a) SWCNTs decorated CFs, inset: high magnification image of SWCNTs@CFs, (b) Fe<sub>2</sub>O<sub>3</sub>-SWCNTs@CF electrode, inset: high magnification image of the prepared electrode, (c), and (d) the corresponding EDS mapping results of the elements Fe, C, and O.

As shown in Figure S10 (a) and (b), successful decoration of CFs with Fe<sub>2</sub>O<sub>3</sub>-SWCNTs is also evidenced by TEM analysis.

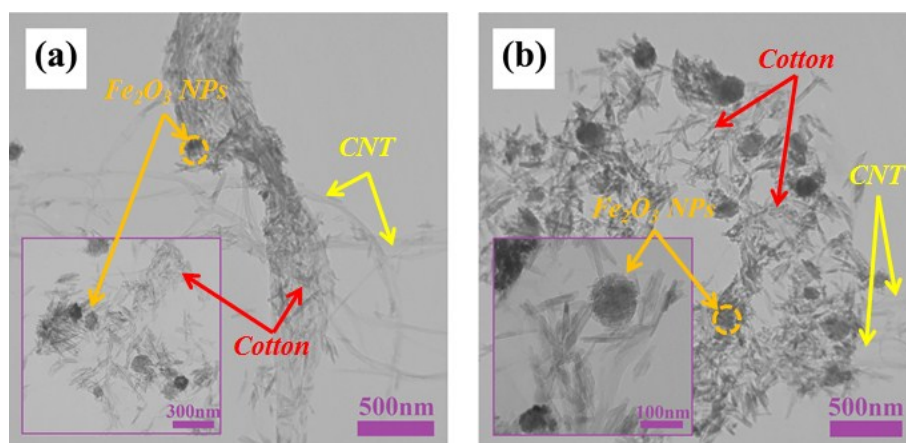


**Figure S10.** (a) and (b) TEM images of Fe<sub>2</sub>O<sub>3</sub>-SWCNTs@CF electrodes.

### *S13 Electrochemical Characterization of Fe<sub>2</sub>O<sub>3</sub>-SWCNTs@CF Electrodes:*

Capacitive performance of the Fe<sub>2</sub>O<sub>3</sub>-SWCNTs@CF negative electrodes were investigated under the same electrochemical conditions used for positive electrodes. CV and GCD measurements were conducted using 3M KOH electrolyte within a potential range of -0.6 to 0 V (vs. Hg/HgO reference electrode) at different scan rates and current densities, respectively. CVs of a Fe<sub>2</sub>O<sub>3</sub>-SWCNTs@CF electrode in different scan rates increasing of 2 to 100 mVs<sup>-1</sup> are shown in Figure S11 (a). The quasi mirror-image symmetry including a pair of well-defined redox peaks provided convincing evidence on the reversible surface film redox reactions<sup>23</sup>. Anodic and cathodic peaks were found to shift slightly from -0.298 and -0.367 V to -0.252 and -0.423 V, respectively, while the scan rate was increased from 2 to 100 mVs<sup>-1</sup>. The Fe<sub>2</sub>O<sub>3</sub>-SWCNTs decorated CF electrode, in this regard, has the benefit of a relatively fast electron transfer kinetics, which resulted in remarkable electrochemical reversibility<sup>24</sup>. Randles-Sevcik curve (Figure S11 (b)) was used to further investigate the charge transfer mechanism where the redox peak currents were plotted as a function of the square root of the potential sweep rates. The diffusion-controlled reversible redox reactions occurred on the surface of the prepared electrodes resulting in a linear variation between the redox peak current and the square root of the potential scan rate within a broad range of the sweep rates<sup>25,26</sup>. Additionally, the correlation between the peak current density and the potential sweep rate was studied for further investigation of the charge transfer mechanism and the results are presented in a log-log plot in Figure S11 (c). A relatively linear behavior with a slope close to 0.5 provided clear evidence that the prepared electrodes receive benefits from the battery-type electrochemical reactions, mainly governed by the diffusion-controlled processes<sup>24,26</sup>.

Frequency response analysis (EIS) was conducted over a broad range of frequencies ranging from 100 kHz to 0.1 Hz under the OCP condition to study the charge transfer mechanism at the electrode/electrolyte interface<sup>24</sup>. The corresponding Nyquist plot and

respective equivalent circuit model are shown in Figure S11 (d). Figure S11 (d) the internal (ESR) resistance, which can be estimated from the first real axis intercept of the Nyquist plot is  $0.596 \Omega$ <sup>23</sup>. Inherent SSA and remarkable wettability, alongside with superior adhesion feature of the unwoven CF network resulted in the negligible ESR<sup>10,27</sup>. As a direct consequence of the fast charge transfer rate, a small semicircle was observed within the high-frequency region<sup>23</sup>. Additionally, with the reasonable diffusion resistance, the Fe<sub>2</sub>O<sub>3</sub>-SWCNTs@CF electrodes exhibited a reasonable capacitive performance within the low-frequency region<sup>24</sup>.

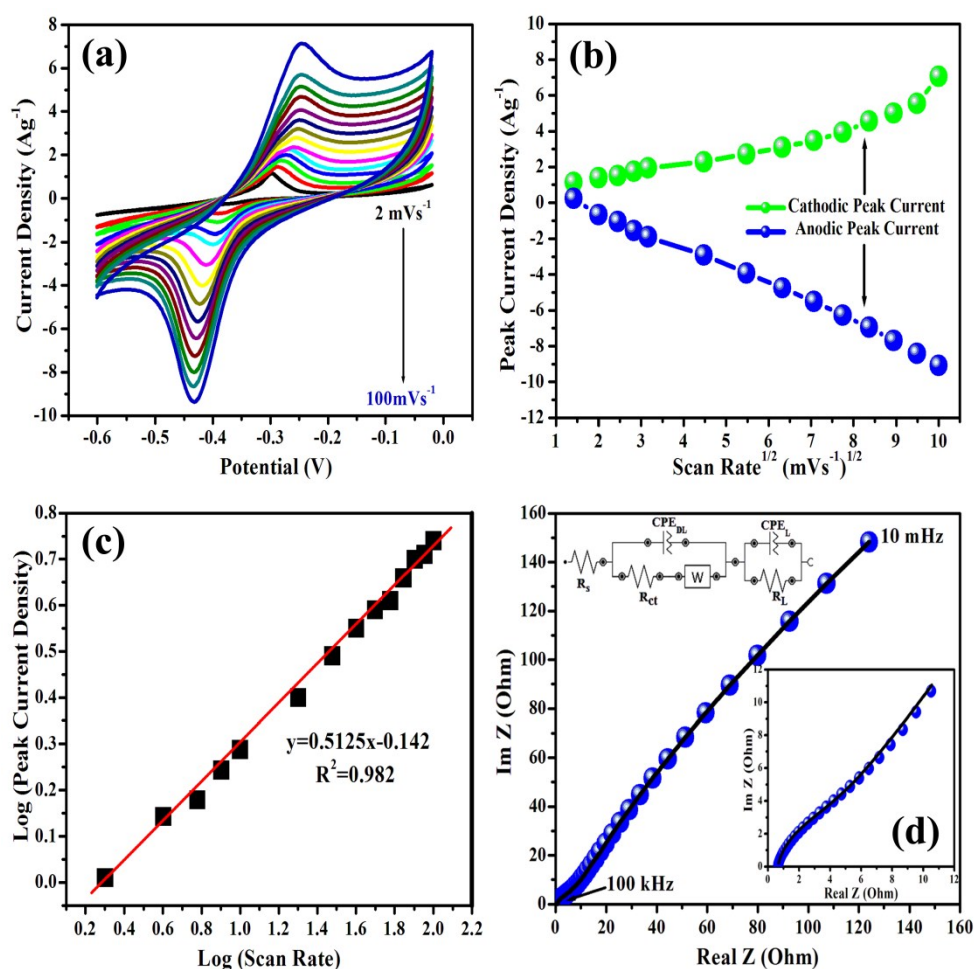


**Figure S11.** (a) The cyclic voltammograms of the Fe<sub>2</sub>O<sub>3</sub>-SWCNTs@CF electrode at different scan rates from 2 to 100 mVs<sup>-1</sup>, (b) peak current density as a function of scan rate, (c) the log-log dependence of the peak current density and the scan rate, and (d) Nyquist plot of Fe<sub>2</sub>O<sub>3</sub>-SWCNTs@CF electrode and the equivalent circuit model corresponded to Nyquist plot over the frequency range of 100 kHz to 0.01 Hz, inset: magnified data in the high-frequency range and equivalent circuit model.

GCD measurements were conducted to further investigate the electrochemical performance of the Fe<sub>2</sub>O<sub>3</sub>-SWCNTs decorated CFs (Figure S12 (a)). There is a good agreement between discharge plateaus and cathodic peaks observed in CV graphs. Gaining the benefit of battery-type behavior, the specific capacities (Cg<sup>-1</sup>) were calculated as a function of current densities, and the results are presented in Figure S12 (b). The specific capacity of the Fe<sub>2</sub>O<sub>3</sub>-SWCNTs@CF electrode is inversely proportional to the current density. As shown in Figure S12 (b), upon increasing the current density from 2.5 to 9.5 Ag<sup>-1</sup>, the specific capacity was decreased slightly from 106.3 to 40.8 Cg<sup>-1</sup>. The prepared electrode, in this regard, retained ~40% of its initial capacity, while the current density increased about 4 times. As a result, the prepared electrode represents a reasonable rate capability and power density<sup>12,26</sup>. As shown in Figure S12 (c), the Fe<sub>2</sub>O<sub>3</sub>-SWCNTs decorated CF electrode exhibited remarkable reversibility with high charge-discharge coulombic efficiency as well as low polarization<sup>28</sup>. Having a crucial significance in the assessment of the electrochemical characterization of the supercapacitor electrodes, the long term cycling stability of the Fe<sub>2</sub>O<sub>3</sub>-SWCNTs@CF based electrode was investigated through 4000 continuous charge-discharge cycles at different current densities increasing from 2.5 to 8.5 Ag<sup>-1</sup> and returning to 2.5 Ag<sup>-1</sup> (Figure S12 (d)). The prepared electrode exhibited a capacity drop of only 11.5 % after 4000 charge-discharge cycles, which revealed the remarkable cycling stability of the Fe<sub>2</sub>O<sub>3</sub>-SWCNTs@CF electrodes<sup>1,29</sup>.

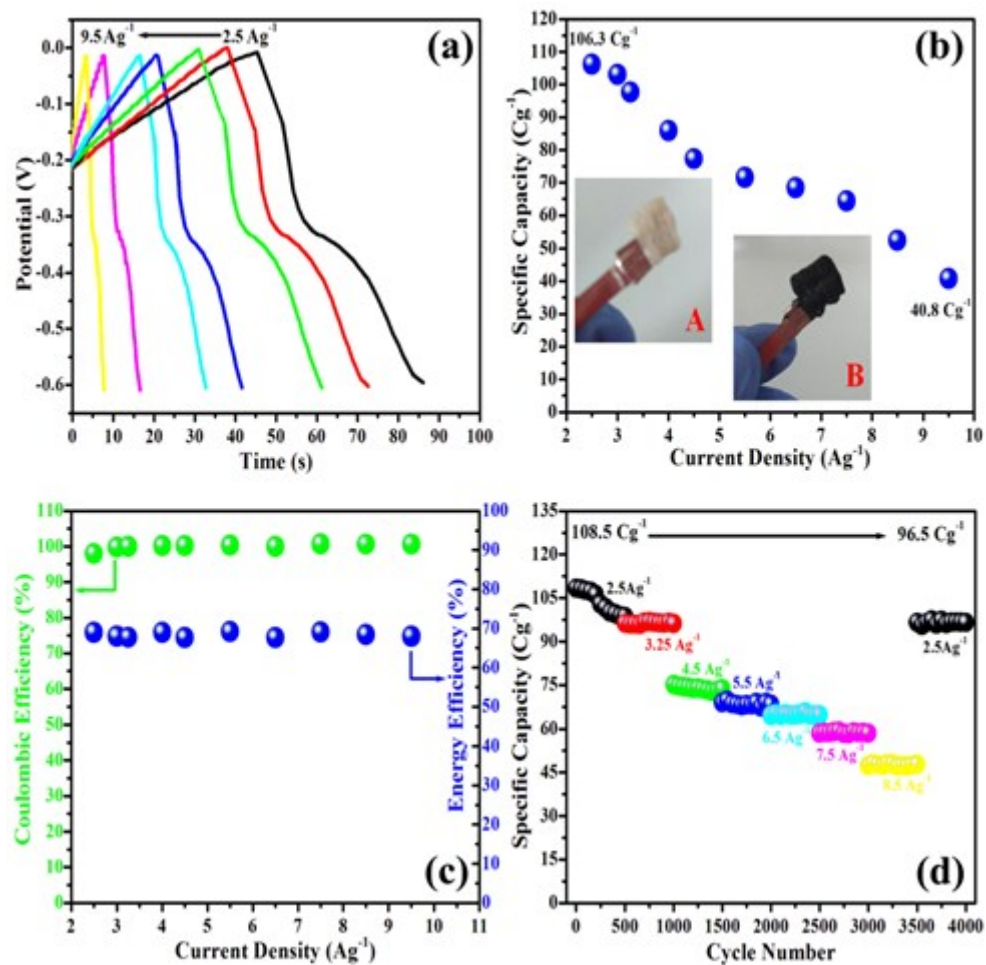


**Figure S12.** (a) GCD curves of the  $\text{Fe}_2\text{O}_3$ -SWCNTs decorated CF electrode at different current densities from 2.5 to 9.5  $\text{Ag}^{-1}$ , (b) the dependence of the gravimetric capacity of the prepared electrode on the applied current density which were calculated from the GCD curves, (c) Coulombic and energy efficiencies of  $\text{Fe}_2\text{O}_3$ -SWCNTs @CF electrode as a function of current density, (d) cycling durability estimation at different current densities from 2.5 to 9.5  $\text{Ag}^{-1}$  and returning to 2.5  $\text{Ag}^{-1}$ . Inset shows the first (in red) and last (in blue) 10 GCD cycles.

#### S14 Cycle Stability of $\text{Fe}_2\text{O}_3$ -SWCNT@CF Negative Electrodes:

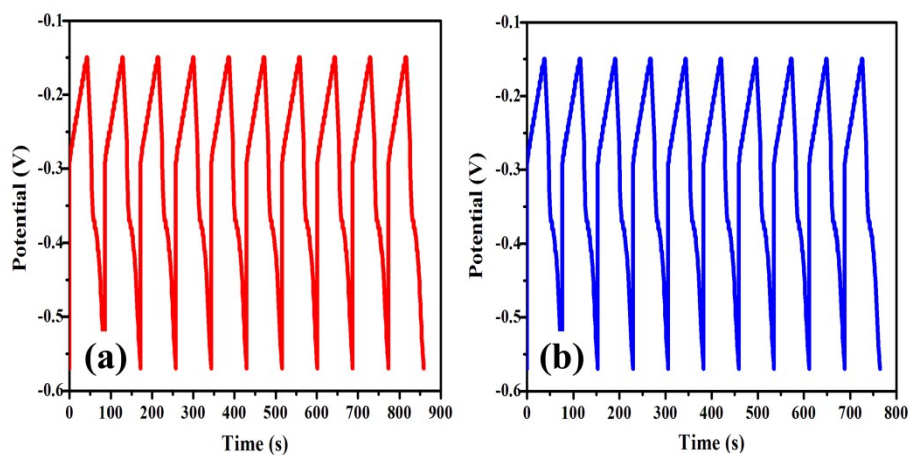


**Figure S13.** (a) The first and (b) last 10 GCD cycles of the  $\text{Fe}_2\text{O}_3$ -SWCNT@CF electrodes at a current density of 2.5  $\text{Ag}^{-1}$ .

**S15 Cycle Stability of Ni-Co-O@CF SSC Devices:**

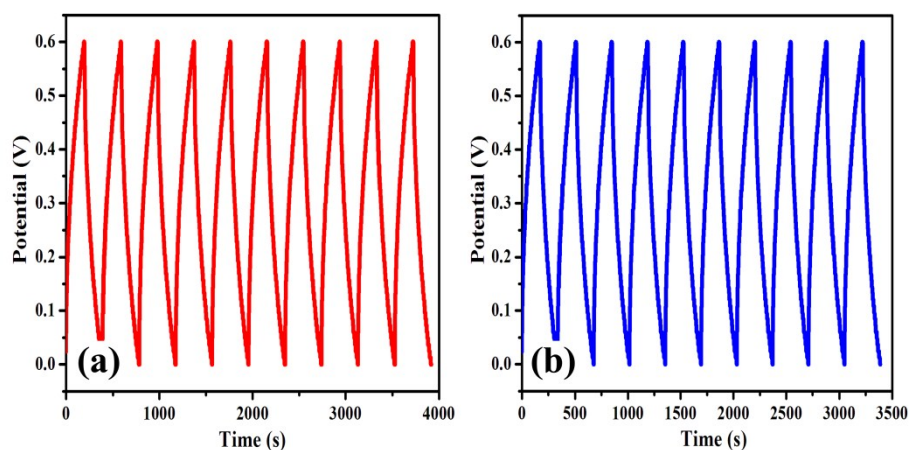


**Figure S14.** (a) The first and (b) last 10 GCD cycles of the all-solid-state Ni-Co-O@CF SSC at a current density of  $1\text{Ag}^{-1}$ .

**S16 Cycle Stability of Ni-Co-O@CF//Fe<sub>2</sub>O<sub>3</sub>-SWCNT@CF ASC Devices:**

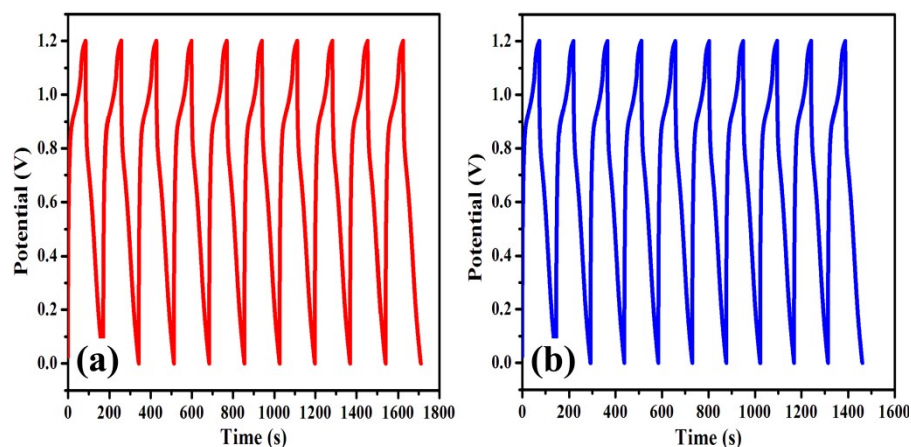


**Figure S15.** (a) The first and (b) last 10 GCD cycles of the all-solid-state Ni-Co-O@CF//Fe<sub>2</sub>O<sub>3</sub>-SWCNT@CF ASC at a current density of  $1\text{Ag}^{-1}$ .

## S17 Comparison of Electrode and Device Properties with Literature

**Table S1.** Electrode properties compared to literature.

Electrode Materials	Electrolyte	C <sub>sp</sub> or Q	Current Load	Cycle Stability	Ref. No
PPy-coated cotton fabric	H <sub>2</sub> SO <sub>4</sub> (1M)	5073 mF/cm <sup>2</sup> (at 1mA/cm <sup>2</sup> )	1-20 mA/cm <sup>2</sup>	90% (after 5000 cycles)	30
aTC	KOH (6M)	1026 mF/cm <sup>2</sup> (at 5 mA/cm <sup>2</sup> )	5-100 mA/cm <sup>2</sup>	-	31
Ni@N NF-CT	KOH (2M)	0.53 mAh/cm <sup>2</sup> (5 mA/cm <sup>2</sup> )	5-25 mA/cm <sup>2</sup>	89.5% (after 1500 cycles)	32
PPy@UIO-66@cotton fabric	Hydroquinone (0.4M)/H <sub>2</sub> SO <sub>4</sub> (1M)	565 F/g (0.8 mA/cm <sup>2</sup> )	0.8-1.4 mA/cm <sup>2</sup>	90% (after 500 cycles)	33
PKCF	H <sub>2</sub> SO <sub>4</sub>	1433 mF/cm <sup>2</sup> (at 1 mA/cm <sup>2</sup> )	1-5 mA/cm <sup>2</sup>	53% (after 5000 cycles)	34
NPCMTs	KOH (6M)	324 F/g (at 1 A/g)	1-20 A/g	98% (after 5000 cycles)	35
Cotton/Au/Ni-Co-S	KOH (1M)	1323 F/g (at 1 A/g)	1-20 A/g	82% (after 2000 cycles)	36
PPy/TiO <sub>2</sub> coated cotton fabric	NaCl (2M)	733 F/g (at 0.6 A/cm <sup>2</sup> )	0.1-0.8 A/g	< 50% (after 500 cycles)	37
CT/Ni/Co-Ni LDH	KOH (2M)	1.26 F/cm <sup>2</sup> (at 2 mA/cm <sup>2</sup> )	2-10 mA/cm <sup>2</sup>	83% (after 1200 cycles)	38
SWCNTs/MnO <sub>2</sub>	LiPF <sub>6</sub> (1M)	140 F/g (at 0.02 mA/cm <sup>2</sup> )	0.02-20 mA/cm <sup>2</sup>	100% (after 120000 cycles)	39
SWCNTs	Li <sub>2</sub> SO <sub>4</sub>	80 F/g (10 μA/g)	0.01-1 mA/g	99% (after 35000 cycles)	40
AC + OLC	Na <sub>2</sub> SO <sub>4</sub>	65 F/g (at 10 mV/s)	-	>90% (after 1000 cycles)	41
GNSs-CC	KOH (6M)	326.8 F/g	-	-	42
MWCNTs/ACT/MnO <sub>2</sub>	Na <sub>2</sub> SO <sub>4</sub> (1M)	247 F/g (at 1 A/g)	1-5 A/g	94.7% (after 2000 cycles)	43
Fe <sub>2</sub> O <sub>3</sub> -SWCNT@CF*	KOH (3M)	106.3 C/g (at 2.5 A/g)	2.5-9.5 A/g	88.5% (after 4000 cycles)	This work
Ni-Co-O@CF**	KOH (3M)	518 C/g (at 3 A/g)	3-15 A/g	92.3% (after 4000 cycles)	This work

\*Due to the battery-type behavior of the positive electrode, the concept of capacity (mAh.g<sup>-1</sup>) was used instead of capacitance (F) as an appropriate metric for the Ni-Co-O@CF electrodes. Accordingly, the specific capacity of the prepared electrodes was about 518 C.g<sup>-1</sup> (which is equal to 863.3 F.g<sup>-1</sup>).

\*\* The specific capacity of the prepared electrodes was about 106.3 C.g<sup>-1</sup> (which is equal to 177.2 F.g<sup>-1</sup>).

C<sub>sp</sub>=Specific Capacitance, Q=Specific Capacity, E<sub>max</sub>= Max Energy Density, P<sub>max</sub>= Max Power Density, PPy=polypyrrole, aTC=activated Textile Carbon, Ni@N NF-CT=Ni-Microspheres@Ni(OH)<sub>2</sub>=Ni-Microspheres@Ni(OH)<sub>2</sub> Nanoflakes Core-Shell on Cotton, ACC=Active Carbon Cloth, PPy@UIO-66=Polypyrrole Nanotubes@Zr-based Metal-Organic Frameworks, PKCF=Polypyrrole/Knitted Cotton Fabric, NPCMTs=N/P Codoped Porous Carbon, CF=Cotton Fiber, LiPF<sub>6</sub>=Lithium hexafluorophosphate, AC=activated carbon, OLC=onion-like carbon, GNSs-CC=Graphene Sheets-Cotton cloth, MWCNTs=Multi-Walled Carbon Nanotubes, ACT=activated carbon textiles.

**Table S2.** Electrochemical properties of ternary Zn-Co-S based ASC devices compared to literature.

Electrode		Electrolyte	$C_{sp}$ or Q (F/g or mAh/g)	$E_{max}$ (Wh/kg)	$P_{max}$ (kW/kg)	Cycle Stability	Ref. No
Positive	Negative						
PPy-coated cotton fabric	PPy-coated cotton fabric	LiCl/PVA	1167.9 mF/cm <sup>2</sup> (at 1 mA/cm <sup>2</sup> )	102.4 $\mu$ Wh/cm <sup>2</sup>	0.39 mW/cm <sup>2</sup>	90% (after 2000 cycles)	30
aTC	aTC	KOH/PVA	153 mF/cm <sup>2</sup> (at 5 mA/cm <sup>2</sup> )	0.42 mWh/cm <sup>3</sup>	10.9 mW/cm <sup>3</sup>	97% (after 10000 cycles)	31
Ni@N NF-CT	ACC	KOH (2M)	1.91 F/cm <sup>2</sup> (at 5 mA/cm <sup>2</sup> )	0.597 mWh/cm <sup>2</sup>	3.68 mW/cm <sup>2</sup>	-	32
PKCF	PKCF	PVA/KOH	450 mF/cm <sup>2</sup> (at 1 mA/cm <sup>2</sup> )	2.3 Wh/kg	57.5 W/kg	70% (after 500 cycles)	34
NPCMT	NPCMT	KOH (6M)	174 F/g (at 0.5 A/g)	10.2 Wh/kg	163.4 W/kg	-	35
Cotton/Au/Ni-Co-S	Cotton/Au/Ni-Co-S	PVA/KOH	141 F/g (at 2 A/g)	40.9 Wh/kg	1.43 kW/kg	80% (after 3000 cycles)	36
SWCNTs/MnO <sub>2</sub>	SWCNTs/MnO <sub>2</sub>	LiPF <sub>6</sub> (1M)	480 mF.cm <sup>-2</sup>	20 Wh/kg	10 kW.kg <sup>-1</sup>	98% (after 8000 cycles)	39
GNSs-CC	GNSs-CC	KOH (6M)	81.7 F/g	11 Wh/Kg	260 W/kg	92% (after 10000 cycles)	42
PCT-V <sub>2</sub> O <sub>5</sub> /ZnCl <sub>2</sub>	PCT-V <sub>2</sub> O <sub>5</sub> /ZnCl <sub>2</sub>	H <sub>2</sub> SO <sub>4</sub> /PVA	2160 mF/cm <sup>2</sup> (at 5 mA/cm <sup>2</sup> )	2.24 mWh/cm <sup>3</sup>	585 mW/cm <sup>3</sup>	100% (after 5000 cycles at 500 mV/s)	44
CNF+AC+MnO <sub>2</sub>	Cotton textile	Nafion-Na <sup>+</sup> /Na <sub>2</sub> SO <sub>4</sub> (1M)	132 F/g (at 0.5 A/g)	11.7 Wh/kg	-	126% (after 10000 cycles)	45
MnO <sub>2</sub> /CCY	MnO <sub>2</sub> /CCY	PVA/KOH	182.94 mF/m <sup>2</sup> (at 20 mV/s)	16.88 $\mu$ Wh/cm <sup>2</sup>	4770 $\mu$ W/cm <sup>2</sup>	~100% (after 5000 cycles)	46
A-CS	A-CS	PVA/KOH	282 F/g (at 0.5 A/g)	22.6 Wh/kg	221 W/kg	81.6% (after 10000 cycles)	47
NPPCC-BC	AC-NF	PVA/KOH	178.9 F/g (at 2 A/g)	45.8 Wh/kg	15.7 kW/kg	88.6% (after 15000 cycles)	48
SWCNTs/MnO <sub>2</sub> /PANI	SWCNTs/MnO <sub>2</sub> /PANI	TBAPF <sub>6</sub> /PC/PMA/ACN	294 F/g (at 1 A/g)	66.4 Wh.kg <sup>-1</sup>	746.5 W.kg <sup>-1</sup>	70% (after 1000 cycles)	49
MnO <sub>2</sub> @PPy	AC@PPy	H <sub>3</sub> PO <sub>4</sub> /PVA	1.21 F/cm <sup>3</sup> (1 mA/cm <sup>3</sup> )	0.0068 Wh/cm <sup>3</sup>	0.0112 W/cm <sup>3</sup>	88% (after 5000 cycles)	50
Ni-Co-O@CF	Ni-Co-O@CF	PVA/KOH	327.2 F/g (at 1 A/g)	16.3 Wh/kg	1200 W/kg	86.6% (after 15000 cycles)	This work
Ni-Co-O@CF	Fe <sub>2</sub> O <sub>3</sub> -SWCNT@CF	PVA/KOH	97.7 C/g (at 1 A/g)	16.3 Wh/kg	3000 W/kg	85% (after 4000 cycles)	This work

$C_{sp}$ =Specific Capacitance, Q=Specific Capacity,  $E_{max}$ = Max Energy Density,  $P_{max}$ = Max Power Density, PCT=Pyrolyzed Cotton Textile, CNF=Carbon Nanofibers, AC=Activated Carbon, CCY=Carbonized Cotton Yarn, A-CS=Architecture of self-doped Carbon Nanofoam, NPPCC-BC=N, P dual-doped Porous Carbon Cloth-Supported Ni-Co Bimetallic Sulfide, AC-NF=Activated Carbon-Nickel Foam, Ni@N NF-CT=Ni-Microspheres@Ni(OH)=Ni-Microspheres@Ni(OH)<sub>2</sub> Nanoflakes Core-Shell on Cotton, ACC=Active Carbon Cloth, PKCF=Polypyrrole/Knitted Cotton Fabric, CF=Cotton Fiber, SWCNT=Single Walled Carbon Nanotubes, MWCNTs=Multi Walled Carbon Nanotube, PANI= polyaniline, TBAPF<sub>6</sub>=tetra butyl ammonium hexafluorophosphate, PMMA=poly methylmethacrylate, PC=propylene carbonate, ACN=acetonitrile, GNSs-CC=Graphene Sheets-Cotton cloth.

## References:

- [1] M. Boota, Y. Gogotsi, *Adv. Energy Mater.* **2019**, *9*, 1802917.
- [2] A. Krause, P. Kossyrev, M. Oljaca, S. Passerini, M. Winter, A. Balducci, *J. Power Sources* **2011**, *196*, 8836-8842.
- [3] W. G. Pell, B. E. Conway, *J. Power Sources* **2004**, *136*, 334-345.
- [4] T. Brousse, D. Bélanger, J. W. Long, *J. Electrochem. Soc.* **2015**, *162*, A5185-A5189.
- [5] Y. Gogotsi, R. M. Penner, *ACS Nano* **2018**, *12*, 2081-2083.
- [6] F. Hekmat, S. Shahrokhian, S. Rahimi, *Nanoscale* **2019**, *11*, 2901-2915.
- [7] H. Wang , H. Yi , X. Chen, X. Wang, *J. Mater. Chem. A* **2014**, *2*, 3223-3230.
- [8] H. Hosseini, S. Shahrokhian, *Appl. Mater. Today* **2018**, *10*, 72-85.
- [9] R. C. Tenent, T. M. Barnes, J. D. Bergeson, A. J. Ferguson, B. To, L. M. Gedvilas, M. J. Heben, J. L. Blackburn, *Adv. Mater.* **2009**, *21*, 3210-3216.
- [10] A. J. Paleo, P. Staiti, A. Brigandi, F. N. Ferreira, A. M. Rocha, F. Lufrano, *Energy Storage Mater.* **2018**, *12*, 204-215.
- [11] X. Peng, H. Liu, Q. Yin, J. Wu, P. Chen, G. Zhang, G. Liu, C. Wu, Y. Xie, *Nat. Commun.* **2016**, *7*, 11782.
- [12] F. Hekmat, B. Sohrabi, M. S. Rahmanifar, A. Jalali, *Appl. Surf. Sci.* **2015**, *341*, 109-119.
- [13] Y. Liu, L. Yu, S. Zhang, J. Yuan, L. Shi, L. Zheng, *Colloids Surf. A* **2010**, *359*, 66-70.
- [14] H. Gao, S. Shaohua Zhang, D. Huang, L. Zheng, Dispersion of multi-wall carbon nanotubes by an ionic liquid-based polyether in aqueous solution. *Colloid Polym. Sci.* **2012**, *290*, 757-762.
- [15] J. Jiao, H. Zhang, L. Yu, X. Wang, R. Wang, *J. Mol. Liq.* **2012**, *171*, 6-10.
- [16] T. Rajkumar, G. Ranga Rao, *Mater. Chem. Phys.* **2008**, *112*, 853-857.
- [17] Y. Kuang, B. Wu, D. Hu, X. Zhang, J. Chen, *J. Solid State Electrochem.* **2011**, *16*, 759-766.
- [18] S. W. Kim, T. Kim, Y. S. Kim, H. S. Choi, H. J. Lim, S. J. Yang, C. R. Park, *Carbon* **2012**, *50*, 3-33.
- [19] N. Hameed, J. S. Church, N. V. Salim, T. L. Hanley, A. Amini, B. L. Fox, *RSC Adv.* **2013**, *3*, 20034-20039.
- [20] M. K. Singh, Y. Kumar, S. A. Hashmi, *Nanotechnology* **2013**, *24*, 465704.
- [21] Y. Lv, A. Liu, Z. Shi, H. Che, J. Mu, Z. Guo, X. Zhang, *Chem. Eng. J.* **2018**, *349*, 397-407.
- [22] M. J. Klein, G. M. Veith, A. Manthiram, *J. Am. Chem. Soc.* **2017**, *139*, 9229-9237.

- [23] Y. Zheng, Z. Lin, W. Chen, B. Liang, H. Du, R. Yang, X. He, Z. Tang, X. Gu, *J. Mater. Chem. A* **2017**, *5*, 5886-5894.
- [24] F. Hekmat, S. Shahrokhian, N. Taghavinia, *J. Phys. Chem. C* **2018**, *122*, 27156-27168.
- [25] B. E. Conway, *Electrochemical Supercapacitors and Their Complementarity to Fuel Cells and Batteries*; Kluwer Academic/Plenum Publishers: New York, U. S., **1999**.
- [26] J. Liu, J. Wang, C. Xu, H. Jiang, C. Li, L. Zhang, J. Lin, Z. X. Shen, *Adv. Sci. (Weinh)* **2018**, *5*, 1700322.
- [27] Y. Lu, W. Wang, Y. Wang, M. Zhao, J. Lv, Y. Guo, Y. Zhang, R. Luo, X. Liu, *Dalton Trans.* **2018**, *47*, 16684-16695.
- [28] P. Wu, S. Cheng, M. Yao, L. Yang, Y. Zhu, P. Liu, O. Xing, J. Zhou, M. Wang, H. Luo, M. Liu, *Adv. Funct. Mater.* **2017**, *27*, 1702160.
- [29] L. Li, Z. A. Hu, N. An, Y. Y. Yang, Z. M. Li, H. Y. Wu, *J. Phys. Chem. C* **2014**, *118*, 22865-22872.
- [30] J. Lv, L. Zhang, Y. Zhong, X. Sui, B. Wang, Z. Chen, X. Feng, H. Xu, and Z. Mao, *Org. Electron.* **2019**, *74*, 59-68.
- [31] W. Zhang, R. Guo, J. Sun, L. Dang, Z. Liu, Z. Lei, and Q. Sun, *J. Colloid Interface Sci.* **2019**, *553*, 705-712.
- [32] Z. Jin, M. Zhou, J. Hu, K. Li, L. Tang, H. Zhao, Z. Cai, and Y. Zhao *J. Alloys Compd.* **2019**, *784*, 1091-1098.
- [33] C. Zhang, J. Tian, W. Rao, B. Guo, L. Fan, W. Xu, and J. Xu, *Cellulose* **2019**, *26*, 3387-3399.
- [34] B. Wang, W. Song, P. Gu, L. Fan, Y. Yin, and C. Wang, *Electrochim. Acta* **2019**, *297*, 794-804.
- [35] L. Li, Y. Zhou, H. Zhou, H. Qu, C. Zhang, M. Guo, X. Liu, Q. Zhang, and B. Gao, *ACS Sustainable Chem. Eng.* **2018**, *7*, 1337-1346.
- [36] H.-T. Wang, Y.-N. Liu, X.-H. Kang, Y.-F. Wang, S.-Y. Yang, S.-W. Bian, and Q. Zhu, *J. Colloid Interface Sci.* **2018**, *532*, 527-535.
- [37] Q. Xu, C. Wei, L. Fan, W. Rao, W. Xu, H. Liang, and J. Xu, *Appl. Surf. Sci.* **2018**, *460*, 84-91.
- [38] H.-T. Wang, C. Jin, Y.-N. Liu, X.-H. Kang, S.-W. Bian, and Q. Zhu, *Electrochim. Acta* **2018**, *283*, 1789-1797.
- [39] L. Hu, M. Pasta, F. L. Mantia, L. F. Cui, S. Jeong, H. D. Deshazer, J. W. Choi, S. M. Han, and Y. Cui, *Nano Lett.* **2010**, *10*, 708-714.
- [40] M. Pasta, F. La Mantia, L. Hu, H. D. Deshazer, and Y. Cui, *Nano Res.* **2010**, *3*, 452-458.

- [41] K. Jost, C. R. Perez, J. K. M. Donough, V. Presser, M. Heon, G. Dion, and Y. Gogotsi, *Energy Environ. Sci.* **2011**, *4*, 5060-5067.
- [42] W.-w. Liu, X.-b. Yan, J.-w. Lang, C. Peng, and Q.-j. Xue, *J. Mater. Chem.* **2012**, *22*, 17245-17253.
- [43] Y. Jiang, X. Ling, Z. Jiao, L. Li, Q. Ma, M. Wu, Y. Chu, and B. Zhao, *Electrochim. Acta*, **2015**, *153*, 246-253.
- [44] D. V. Lam, S. Won, H. C. Shim, J.-H. Kim, and S.-M. Lee, *Carbon* **2019**, *153*, 257-264.
- [45] A. J. Paleo, P. Staiti, A. M. Rocha, G. Squadrito, and F. Lufrano, *J. Power Sources* **2019**, *434*, 226735.
- [46] S. Ullah, J. Yu, H. Liu, W. Iqbal, B. Yang, C. Li, C. Zhu, and J. Xu, *Appl. Surf. Sci.* **2019**, *487*, 180-188.
- [47] Z. Li, S. Gao, H. Mi, C. Lei, C. Ji, Z. Xie, C. Yu, and J. Qiu, *Carbon* **2019**, *149*, 273-280.
- [48] M. Hua, T. Chen, and H. Ma, *ACS Appl. Energy Mater.* **2019**, *2*, 4316-4324.
- [49] R. Yuksel and H. E. Unalan, *Int. J. Energy Res.* **2015**, *39*, 2042-2052.
- [50] Y. Lu, W. Wang, Y. Wang, M. Zhao, J. Lv, Y. Guo, Y. Zhang, R. Luo, and X. Liu, *Dalton Trans.* **2018**, *47*, 16684-16695.